

#### An experimental and numerical study on the cracking of alkali-activated slag pastes induced by water immersion

Liu, Chen; Xie, Jinbao; Li, Zhenming; Ye, Guang

DOI

10.1016/j.cemconres.2025.107877

**Publication date** 

**Document Version** Final published version

Published in

Cement and Concrete Research

Citation (APA)

Liu, C., Xie, J., Li, Z., & Ye, G. (2025). An experimental and numerical study on the cracking of alkaliactivated slag pastes induced by water immersion. *Cement and Concrete Research*, *193*, Article 107877. https://doi.org/10.1016/j.cemconres.2025.107877

Important note

To cite this publication, please use the final published version (if applicable). Please check the document version above.

Copyright

Other than for strictly personal use, it is not permitted to download, forward or distribute the text or part of it, without the consent of the author(s) and/or copyright holder(s), unless the work is under an open content license such as Creative Commons.

Please contact us and provide details if you believe this document breaches copyrights. We will remove access to the work immediately and investigate your claim.

ELSEVIER

Contents lists available at ScienceDirect

#### Cement and Concrete Research

journal homepage: www.elsevier.com/locate/cemconres



# An experimental and numerical study on the cracking of alkali-activated slag pastes induced by water immersion

Chen Liu<sup>a</sup>, Jinbao Xie<sup>a</sup>, Zhenming Li<sup>b,c,\*</sup>, Guang Ye<sup>a,\*\*</sup>

- a Department of Materials and Environment (Microlab), Faculty of Civil Engineering and Geoscience, Delft University of Technology, 2628 CN Delft, the Netherlands
- <sup>b</sup> School of Civil and Environmental Engineering, Harbin Institute of Technology, 518055 Shenzhen, China
- <sup>c</sup> Guangdong Provincial Key Laboratory of Intelligent and Resilient Structures for Civil Engineering, Harbin Institute of Technology, 518055 Shenzhen, China

#### ARTICLE INFO

# Keywords: Alkali-activated slag Cracking Water immersion Pore pressure Stress concentration Finite element simulation

#### ABSTRACT

Cementitious materials can achieve desirable strength development and reduced cracking potential under moist or immersed conditions. However, in this work, we found that alkali-activated slag (AAS) pastes can crack underwater, with a higher silicate modulus showing more pronounced cracking. Chemically, the C-(N-)A-S-H gel in the paste with a higher silicate modulus showed a higher Na/Si ratio and a higher leaching loss of Na, which led to more significant structural changes and gel deterioration underwater. This triggered the propagation of cracks initially present in the material. Physically, the paste with a higher silicate modulus featured a denser microstructure, lower water permeability and higher pore pressure, which resulted in a steeper gradient of pore pressure in the matrix. Consequently, the concentration of tensile stress was simulated at the centre and the corner of the cross-section of the sample. As this simulated concentrated stress exceeded the flexural strength of AAS pastes, significant fractures at the centre and spalling at the corner occurred, consistent with the experimental observation. This work not only elucidated the cracking mechanisms of AAS materials underwater but also provided new insights into mixture designs for these materials under high-humidity conditions.

#### 1. Introduction

Leaching, the process by which constituents of solid materials are released into liquid environments, is seemingly inevitable for structures serving under complex conditions, e.g., roads, buildings, bridges, tunnels and underground infrastructure. In PC-based materials, the pH of the pore solution typically ranges from 12.5 to 13.9 [1,2], depending on various factors such as cement types, water-binder ratios, and initial alkali contents. Since hydrates in PC-based materials exhibit thermodynamic stability under alkaline conditions, external water can be regarded as a form of "chemical corrosion", leading to the dissolution of calcium hydroxide and decalcification of C-S-H gels [3-5]. However, as a hydraulic material, PC hardens and gains strength through the reaction with water. Water curing has been verified as effective in enhancing the hydration degree of cement [6], which eventually contributes to reduced shrinkage, improved mechanical properties and durability. Consequently, water exposure is generally beneficial for PC-based materials.

In contrast to PC-based materials, alkali-activated materials (AAMs)

are synthesized through the alkali activation of aluminosilicate precursors, including industrial by-products, mineral residues, and agricultural wastes [7–10]. The reaction of precursors and the formation of microstructure are significantly dependent on the pH of the pore solution. The infiltration of external water into AAMs can lower the pore solution alkalinity, which would hinder the reaction of precursors, the formation of reaction products and the strength development of AAMs [11,12]. Besides, it is found that the C-(N-)A-S-H gels in AAS pastes can decompose after long-term water immersion [11]. Consequently, reduced reactions of producers and gel decomposition lead to coarsened microstructures and reduced long-term mechanical properties and durability [11,13–15].

Furthermore, an increasing number of studies have indicated that external water can even trigger the formation of cracks in AAMs, especially for AAS materials. Hubler et al. [16] investigated the impact of nucleation seeding on the reaction and compressive strength of AAS paste. Their findings revealed a continuous increase in the compressive strength of AAS pastes under sealed conditions, but a decrease trend subjected to underwater conditions due to cracking. They attributed this

E-mail addresses: c.liu-12@tudelft.nl (C. Liu), zhenmingli@hit.edu.cn (Z. Li), g.ye@tudelft.nl (G. Ye).

<sup>\*</sup> Correspondence to: Z. Li, School of Civil and Environmental Engineering, Harbin Institute of Technology, 518055 Shenzhen, China.

<sup>\*\*</sup> Corresponding author.

problem to the differential stresses resulting from chemical and autogenous shrinkage. Maghsoodloorad et al. [17] observed severe cracks in alkali-activated phosphorus slag pastes upon hydrothermal curing. They attributed these cracks to non-uniform shrinkage caused by the uneven distribution between reaction products and unreacted slag under hydrothermal conditions. Hwang et al. [18] also identified cracks in waterimmersed AAS pastes. Besides, such cracking problems became more pronounced in slag with an increased content of MgO. They assumed that a high MgO content in slag promotes the formation of hydrotalcite, which can result in the expansion of the matrix and an increased likelihood of cracking. In a previous work [19], we compared the flexural strength of AAS mortars under different curing conditions. The results indicated a decline in the flexural strength of sodium silicate-based mortars over time when exposed to high-humidity curing conditions. Given that the flexural strength was sensitive to surface cracks, this reduction may also relate to the cracking issue. Accordingly, previous studies have confirmed the occurrence of undesirable cracks and reduced mechanical properties of AAS materials under wet or immersed conditions. However, the underlying mechanisms remain inconclusive. In practice, water exposure is unavoidable, whether during initial curing periods to reduce shrinkage or in underground, marine or normal outdoor conditions. Therefore, to promote the application of AAS materials, a deeper understanding of this cracking issue is essential for optimizing the mixture design of these materials.

In this study, AAS pastes were produced using alkaline activators with different silicate moduli (0, 0.5, 1, 1.5). Firstly, the compressive and flexural strength of pastes cured with and without water immersion were compared. Secondly, phase assemblage, paste chemistry, gel structure and leaching stability of gels in AAS pastes with different silicate moduli were systematically examined to analyze the change of chemical properties of AAS pastes before and after water immersion. Then, pore volume, pore size distribution and saturation degree were determined to understand the transport properties of AAS pastes. These physical parameters served as inputs for modelling the water transport, pore pressure and internal tensile stress of AAS materials subjected to water immersion. Based on the experimental and modelling results, we finally clarified the cracking mechanisms of AAS pastes subjected to water immersion from both chemical and physical prospectives and proposed some potential solutions to address this issue.

#### 2. Methodology

#### 2.1. Outline of this study

The outline of this study is presented in Fig. 1. In terms of chemical aspects, firstly, the phase assemblage of AAS pastes before and after immersion in deionized water was analyzed using X-ray diffraction (XRD), which was used to identify any newly formed phases during immersion. Secondly, the paste chemistry of AAS pastes before water immersion was measured by scanning electron microscopy (SEM) with energy-dispersive X-ray (EDX) detectors. Thirdly, the leaching test on powdered AAS pastes was conducted to specifically investigate the leaching behaviour of gels in different AAS pastes. Finally, Fourier-transform infrared spectroscopy (FTIR) was performed to assess the structural change of gels in AAS pastes induced by leaching.

As for physical aspects, a transport-mechanical model was employed to simulate the water penetration induced by capillary suction of unsaturated pastes and the resulting distribution of pore pressure and internal tensile stress in AAS pastes using finite element method (FEM). To gain the input, the water content (or saturation degree) of pastes before water immersion was measured. The porosity and pore size distribution of pastes were characterized by mercury intrusion porosimetry (MIP) and  $\rm N_2$  absorption test. Eventually, based on experimental and simulated results in this work, some potential mitigation strategies to address the cracking issue of AAS materials subjected to water-exposed conditions were proposed.

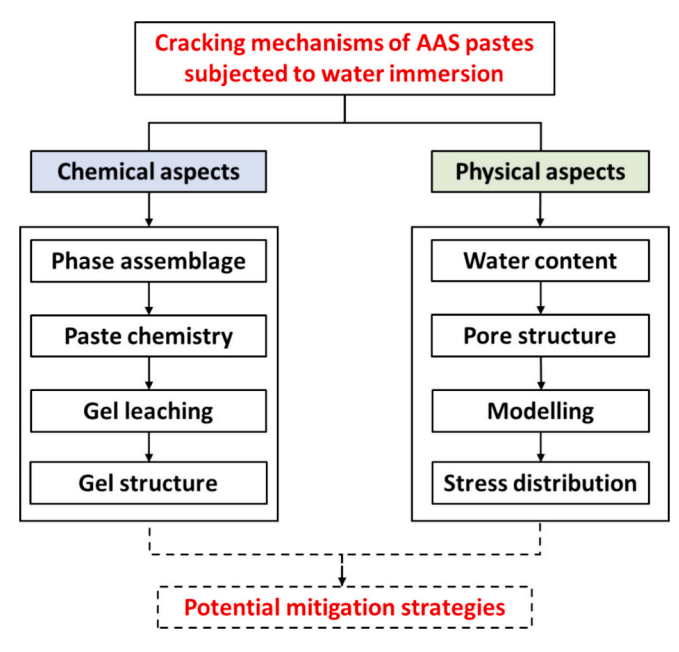


Fig. 1. Outline of this work.

#### 2.2. Materials and mixtures

The chemical composition of slag was determined by X-ray fluorescence (XRF), as presented in Table 1. The particle size of slag ranged from 0.5 to 50  $\mu$ m, with a d<sub>50</sub> of 18.2  $\mu$ m. Four types of activators with silicate modulus (SiO<sub>2</sub>/Na<sub>2</sub>O) of 0, 0.5, 1 and 1.5 were used in this study, which were prepared using NaOH solution (50 wt%), Na<sub>2</sub>SiO<sub>3</sub> solution (8.25 wt% Na<sub>2</sub>O, 27.5 wt% SiO<sub>2</sub>, and 64.25 wt% water), and deionized water.

The mixture design of AAS pastes is presented in Table 2. The water binder ratio and alkali dosage of four AAS pastes were 0.43 and 5%, respectively. The slag was activated using alkali activators with different silicate moduli, referred to as  $m=0,\,0.5,\,1$  and 1.5, respectively. This aimed to cover the range of silicate moduli used in AAS materials as much as possible. The fresh AAS pastes were prepared at a room temperature of 20 °C using a Hobart mixer. The paste was then cast in 4 cm  $\times$  4 cm  $\times$  16 cm moulds for the flexural and compressive strength tests, and polyethene bottles ( $\phi$  35 mm  $\times$  70 mm) for other characterizations.

#### 2.3. Experimental methods

#### 2.3.1. Flexural and compressive strength tests

The 4 cm  $\times$  4 cm  $\times$  16 cm AAS prisms were initially sealed for 7 d and subsequently exposed to either sealed or water-immersed conditions for an additional 7 d. The strength of specimens labelled as "7 s", "7 s + 7 s" and "7 s + 7w" was measured. These labels referred to "7 d of sealed curing", "7+7 d of sealed curing" and "7 d of sealed curing followed by 7 d of water immersion", respectively. For flexural strength, a loading rate of 0.05 kN/s was applied, with three replicates per mixture. Following the flexural strength test, the obtained six halves of prisms were used to measure compressive strength, using a loading rate of 2.4 kN/s. The detailed procedure of flexural and compressive strength tests was shown in standard NEN-EN 196–1 [20].

#### 2.3.2. XRD test

XRD was conducted using a Bruker D8 Advance diffractometer applying CuK $\alpha$  (1.54 Å) radiation. The AAS samples were first sealed in the aforementioned polyethene bottles for 7 d. Then, the samples were crushed into approximately 2–4 mm pieces before being exposed to deionized water for 7 d. Finally, the piece samples after exposure were immersed in isopropanol and ground into fine powder to stop the

Table 1 Chemical composition of slag (wt%).

	CaO	$Al_2O_3$	$SiO_2$	MgO	$Fe_2O_3$	$SO_3$	K <sub>2</sub> O	$TiO_2$	other	LOI
Slag	40.2	13.4	32.3	9.2	0.4	1.6	0.5	1.6	0.5	0.3

LOI = loss on ignition at 1000  $^{\circ}$ C.

**Table 2**Mixture proportions of AAS pastes.

	Slag (g)	SiO <sub>2</sub> (mol)	Na <sub>2</sub> O (mol)	Water (g)
m = 0	1000	0	0.8	430
m = 0.5	1000	0.4	0.8	430
m=1	1000	0.8	0.8	430
m=1.5	1000	1.2	0.8	430

reaction. After being dried in a vacuum oven at 25  $^{\circ}$ C for 7 d, the powdered sample underwent scanning within the range of 5–70 $^{\circ}$  with a step size of 0.02 $^{\circ}$  and a swell time of 5 s per step.

#### 2.3.3. EDX spectroscopy

The elemental composition of gels in AAS pastes was determined using an FEI QUANTA FEG 650 environmental scanning electron microscope (ESEM) with EDX spectroscopy. The 7 d sealed bulk samples were immersed in isopropanol for 7 d and then vacuum-dried for 7 d. Then, the samples were impregnated with low-viscosity epoxy resin. After the resin was solidified, the samples were polished successively with #320, #800 and #1200 silicon carbide papers, followed by polishing clothes with 3 and 1  $\mu m$  diamond paste. The well-polished samples were coated with carbon at a thickness of 10 nm. An accelerating voltage of 10 kV and a working distance of 10 mm were used during the test.

#### 2.3.4. ICP-OES and FTIR tests

Inductively coupled plasma-optical emission spectrometry (ICPOES) was performed to investigate the leaching behaviour of gels in AAS pastes using a PerkinElmer Optima 5300DV. To mitigate the impact of the pore solution and focus solely on the gels, the 7 d reaction-arrested powdered samples were employed. 0.500 g ( $\pm$  0.03) of samples were added to a polyethene bottle containing 30.0 g ( $\pm$  0.1) of deionized water. After standing for 7 d, the leachate was filtered and the concentration of Si, Al, Ca and Na was measured. The solid residue was dried in a vacuum oven at 25 °C. After that, FTIR was carried out to detect the structural change of gels with and without leaching. The FTIR measurement was performed on a Nicolet  $^{\rm TM}$  iS50 FTIR Spectrometer, with a wavenumber ranging from 600 to 4000 cm $^{-1}$  and a resolution of 4 cm $^{-1}$ .

#### 2.3.5. MIP and $N_2$ absorption tests

MIP was conducted using a Micrometrics PoreSizer 9500 to obtain the open porosity and pore size distribution of AAS pastes. The correlation between pore diameter (*D*) and pore pressure (*P*) is built by the Washburn equation [21] as presented in Eq. (1).

$$P = -\frac{4\gamma cos\theta}{D} \tag{1}$$

where the  $\gamma$  is the surface tension of mercury, 0.485 N/m at 25 °C;  $\theta$  is the contact angle between samples and mercury, 141° in this work.

Three procedures were involved in each measurement, including mercury intrusion at low pressure from 0 to 0.170 MPa; mercury intrusion at high pressure from 0.170 to 210 MPa; and mercury extrusion. According to Eq. (1), the pore diameter that can be detected ranges from 400  $\mu m$  to 7 nm. The "effective porosity", "threshold/critical pore diameter" and "ink-bottle porosity" can be also deduced from the MIP results as presented in Fig. 2. Effective porosity refers to pore volume that is interconnected and capable of contributing to fluid flow or

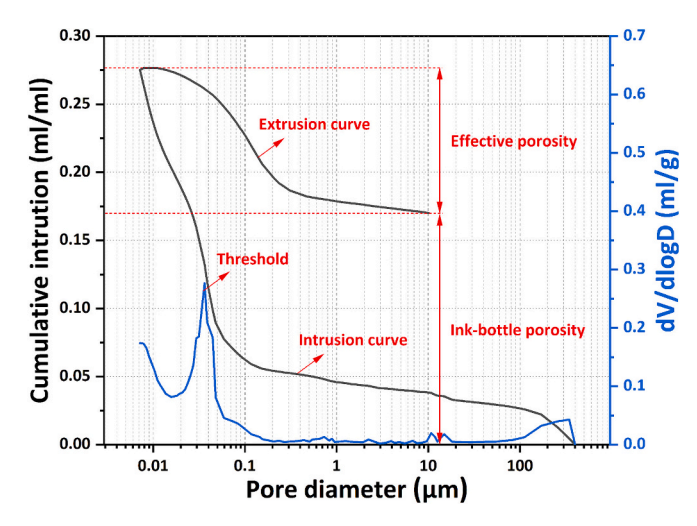


Fig. 2. Schematic representation of effective porosity, ink-bottle porosity and threshold pore diameter obtained from MIP results.

permeability. "Ink-bottle" is connected to the surface or other pores through narrower throats. These pores can retain mercury due to the smaller throats that prevent its egress during pressure release. The threshold/critical pore diameter corresponds to the point on the intrusion curve where a significant increase in cumulative intrusion is observed, indicating the entry of mercury into a dominant pore size range. Since the pore diameter of m=1 and m=1.5 AAS pastes was below the detecting limit of MIP equipment,  $N_2$  absorption test was conducted by a Micrometrics Gemini VII 2390 V1.03 to identify pores ranging from 0.3 nm to 300 nm.

#### 2.3.6. Water content test

The water content (or saturation degree) of 7 d sealed AAS paste was measured before water immersion. The samples were sealed for 7 d and then crushed into 2–4 mm pieces. The initial mass of samples was recorded as  $m_i$  (accurate to 0.001 g). Then, the samples were dried in an oven at 40 °C for 48 h to a constant weight ( $m_d$ ). Finally, the samples were fully submerged in deionized water under vacuum conditions to a constant weight ( $m_s$ ). It should be noted that the leaching loss of Na ( $m_{Na}$ ) was also taken into account during the test, due to its significant leaching amount [11]. The ion concentration of Na in the leachate was measured and the leaching amount was calculated. As a result, the saturation degree of AAS samples can be calculated as Eq. (2).

$$S = \frac{m_i - m_d}{m_s - m_d + m_{Na}} \times 100\% \tag{2}$$

Using this method, the saturation degrees of AAS pastes with m=0, 0.5, 1 and 1.5 after 7 d of sealed curing were determined to be 94.6%, 93.8%, 92.3% and 90.2%, respectively.

#### 2.4. Numerical simulation

During the initial 7 d of sealed curing, the water content (or saturation degree) in the AAS pastes decreased due to self-desiccation. Upon water immersion, the unsaturated paste can absorb water through capillary suction. Given the rapid progression of capillary suction, experimental methods such as computed tomography (CT) scans are not

feasible for real-time observation due to their time-consuming nature. Consequently, we investigated this phenomenon using simulation methods. A schematic diagram of simulation procedures on the cross-section of AAS pastes is depicted in Fig. 3. A cross-section at the middle of the AAS prism was selected for simulation (Fig. 3A). The water ingress caused by capillary suction resulted in a dynamic redistribution of water content over time (Fig. 3B). This redistribution influenced the pore pressure within the matrix (Fig. 3C), which disrupted static equilibrium and led to an uneven internal stress distribution (Fig. 3D). FEM was employed to simulate the entire process. Before presenting the simulation model, it is essential to understand some fundamental concepts underlying the methodology.

#### 2.4.1. Governing equation

Richards' equation describes the water flow in an unsaturated porous medium, driven by gravity and capillary force, while neglecting the movement of the non-wetting phase, typically air [4,5]. Richards' equation is a simplified form of the standard two-phase flow model for gas and liquid phases in a porous medium. It assumes that the pressure gradient needed to drive the flow of the gas phase can be neglected, owing to the significant mobility contrast between the water and gas phases. Generally, Richards' equation is presented in three different forms: (1) the "mixed form", which incorporates both water saturation and pressure head; (2) the "head-based form", which is expressed entirely in terms of pressure head; and (3) the "saturation-based form", which focuses on water saturation rather than pressure head. In this case, water movement in AAS pastes is driven by the capillary suction (pore pressure). The pressure head was not considered in this study, as it was neglectable compared to capillary pressure. The transient state formulation of Richards' equation used in this study is expressed as:

$$\frac{\partial \theta}{\partial t} = \nabla \bullet (K_{\theta} \nabla p) \tag{3}$$

where  $\theta$  is the water content,  $K_{\theta}$  is the unsaturated water permeability of pastes, and p is the pore pressure.

If the capillary diffusivity ( $D_{\theta}$ ) is defined as Eq. (4), the Richards' equation can be also formulated as Eq. (5).

$$D_{\theta} = K_{\theta} \frac{\partial p}{\partial \theta} \tag{4}$$

$$\frac{\partial \theta}{\partial t} = \nabla \bullet (D_{\theta} \nabla \theta) \tag{5}$$

In an unsaturated condition without external pressure, the pore pressure  $p(\theta)$  is the main driving force of water absorption and transport, which can be expressed as a function of water content  $(\theta)$  according to [22]:

$$p(\theta) = \frac{2CB\gamma\cos\theta_c}{\ln\left(1 - \frac{\theta}{\varphi}\right)} \tag{6}$$

where C is an empirical constant (2.15, as assumed in [23]), B [1/mm] is the Rileigh-Ritz pore size distribution constant, which is assigned to the peak value of pore size distribution on a logarithmic scale [24] and can be fitted from the pore diameter distribution according to MIP and N<sub>2</sub> absorption results,  $\gamma$  is the liquid-vapour interfacial energy (7.2 × 10<sup>-5</sup> N•mm<sup>-1</sup>),  $\theta_c$  is the equilibrium contact angle between the liquid and the solid ( $\cos\theta_c = 0.94$ ),  $\varphi$  is the open porosity of porous media.

Zhou et al. [24] studied the correlation between unsaturated water permeability ( $K_{\theta}$ ), open porosity ( $\varphi$ ) and water content ( $\theta$ ) in PC-based materials. Given that AAS materials share a similar morphology of pore distribution with PC-based materials [25],  $K_{\theta}$  of AAS pastes can be calculated via Eq. (7).

$$K_{\theta} = \frac{\varphi^2}{50B^2\mu} \left( 1 - \left[ 1 - \ln\left(1 - \frac{\theta}{\varphi}\right) \right] \left(1 - \frac{\theta}{\varphi}\right) \right)^2 \tag{7}$$

where  $\mu$  is the dynamic viscosity of water.

By substituting Eqs. (6) and (7) into Eq. (4) and performing some algebraic manipulations, the resulting expression for the capillary diffusivity  $(D_{\theta})$  is obtained:

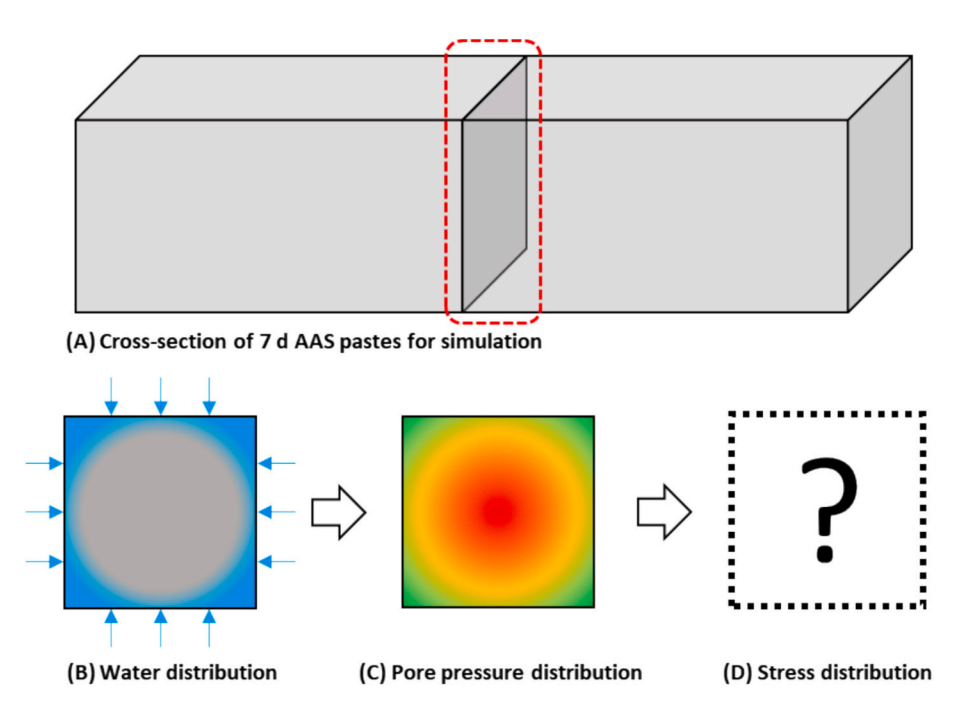


Fig. 3. Schematic diagram of simulation procedures. The blue part in (B) refers to the water-percolated part resulting from the capillary suction. The pore pressure in (C) is indicated by the colour gradient, following the sequence of red (high pressure), orange (moderate pressure), and green (low pressure). (For interpretation of the references to colour in this figure legend, the reader is referred to the web version of this article.)

$$D_{\theta} = \frac{C\gamma \cos\theta_{c}}{25B\mu} \frac{\varphi^{2}}{(\varphi - \theta)\ln^{2}\left(1 - \frac{\theta}{\varphi}\right)} \left(1 - \left[1 - \ln\left(1 - \frac{\theta}{\varphi}\right)\right] \left(1 - \frac{\theta}{\varphi}\right)\right)^{2}$$
(8)

#### 2.4.2. Numerical implementation

The flowchart of the transport-mechanical model is presented in Fig. 4. This model integrates water transport and mechanical stress simulations to analyze the behaviour of AAS pastes during water immersion.

2.4.2.1. Water transport model. A 2D finite element model was developed to simulate water transport across a 4 cm  $\times$  4 cm cross-section in the middle of the prism (Fig. 3A). This model was implemented using ABAQUS software, which has been validated in previous studies for simulating water and chloride diffusion in cementitious materials [26–28]. Water transport in porous media was modelled using the heat transfer module in ABAQUS. This approach leveraged the similarity between water transport (based on Fick's second law) and heat transfer phenomena. The comparison between heat transfer and water transport is shown in Appendix A Eqs. (S1) and (S2), and Table S1.

The non-steady state of unsaturated water transport was simulated using a 4-node linear quadrilateral element. The porosity and water content of AAS pastes obtained from experiments were used as inputs. Since the samples were initially cured under sealed conditions before being exposed to water, the porosity and water content were assumed to be homogeneously distributed across the entire simulated cross-section. The pore structure was assumed to be constant during 1 h water immersion, and all the pores in the media were permeable during capillary suction. According to Eq. (8), the capillary diffusivity  $D_{\theta}$  of AAS pastes is calculated based on variations in water content  $\theta$ . Since the saturation degree  $(\theta/\varphi)$  in Eq. (8) cannot reach 1, it was capped at 0.999 for calculations. Appendix A Fig. S3 shows the relationship between  $D_{\theta}$  and water content  $\theta$  of AAS pastes with different silicate moduli. Detailed input parameters for the water transport model of four AAS pastes are listed in Appendix A Table S2. Given the observed cracking in m = 1.5 paste prisms after 1 h of water immersion (Appendix A Fig. S1), we concentrated on simulating the water content distribution during the first hour for all four pastes. The simulated water content distribution at 1 h was converted to pore pressure distribution using Eq. (6). In the water transport model, an iterative nonlinear solver based on the Newton-Raphson method was implemented in ABAQUS to address the material nonlinearity problem.

#### 2.4.2.2. Mechanical model. Due to the shrinkage of AAS pastes during

sealed curing, the pore pressure-induced stress was assumed to act towards the centre of the cross-section. To incorporate pore pressure into the model, it was decomposed into its stress components  $(\sigma_x, \sigma_y, \tau_{xy})$ , as illustrated in Fig. 5. The cross-section was divided into a 33  $\times$  33 grid (Fig. 5A) following a mesh sensitivity analysis, which is shown in Appendix A Fig. S4. For each unit, the pore pressure formed an angle  $\theta$  with the global X-axis. Fig. 5B and C depict the decomposition of the pore pressure into normal stress  $(\sigma_\alpha)$  and tangential stress  $(\tau_\alpha)$  on any inclined section. These stresses were related to the unit's normal stresses in the x-direction  $(\sigma_x)$  and y-direction  $(\sigma_y)$ , as well as the in-plane shear stress  $(\tau_{xy})$  along the xy-axis, as shown in Eqs. (9) and (10).

$$\sigma_{\alpha} = \frac{\sigma_{x} + \sigma_{y}}{2} + \frac{\sigma_{x} - \sigma_{y}}{2} \cos 2\theta - \tau_{xy} \sin 2\theta \tag{9}$$

$$\tau_{\alpha} = \frac{\sigma_{x} - \sigma_{y}}{2} \sin 2\theta + \tau_{xy} \cos 2\theta \tag{10}$$

The sum of the normal stresses on two mutually perpendicular planes remains constant, i.e.  $\,$ 

$$\sigma_{\alpha} + \sigma_{\alpha+90^{\circ}} = \sigma_{x} + \sigma_{y} \tag{11}$$

When only principal stresses are considered,  $\tau_{\alpha} = 0$ . Therefore, based on Eqs. (9)–(11), we can derive  $\sigma_{x}$ ,  $\sigma_{y}$ , and  $\tau_{xy}$  as

$$\begin{cases} \sigma_{x} = \sigma_{a} \cdot \cos^{2}\theta + \sigma_{a+90^{\circ}} \cdot \sin^{2}\theta \\ \sigma_{y} = \sigma_{a} \cdot \sin^{2}\theta + \sigma_{a+90^{\circ}} \cdot \cos^{2}\theta \\ \tau_{xy} = (\sigma_{a+90^{\circ}} - \sigma_{a}) \cdot \sin\theta \cos\theta \end{cases}$$

$$(12)$$

Since the pore pressure is directed towards the centre,  $\sigma_{\alpha+90^{\circ}}=0.$  Thus,

$$\begin{cases}
\sigma_{x} = \sigma_{a} \cdot \cos^{2}\theta \\
\sigma_{y} = \sigma_{a} \cdot \sin^{2}\theta \\
\tau_{xy} = -\sigma_{a} \cdot \sin\theta \cos\theta
\end{cases}$$
(13)

These stress components ( $\sigma_x$ ,  $\sigma_y$ , and  $\tau_{xy}$ ) were applied to the ABA-QUS model as predefined fields for each material unit. A Python script was used in ABAQUS to apply pore pressure, extracted from the water transport model, to each unit in the mechanical model, which is provided in Appendix B.

Cementitious materials are typically with high brittleness and low ductility, making them more sensitive to tensile stress than compression [29–31]. The investigation of tensile strength is crucial when addressing issues of cracking and fracture. Therefore, we simulated the distribution of internal tensile stress in the cross-section of AAS pastes at 1 h of water immersion. Here, the Direct Solver within the static analysis module was used to simulate this process, utilizing a 4-node bilinear plane stress quadrilateral element. In the mechanical model, displacement boundary

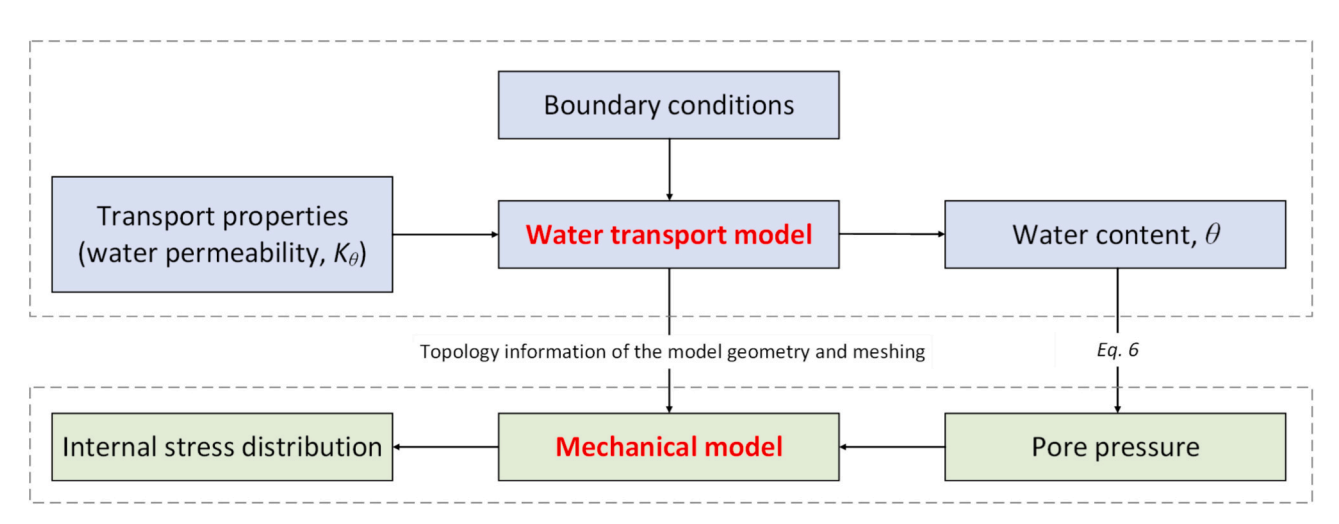


Fig. 4. Flowchart of the transport-mechanical model.

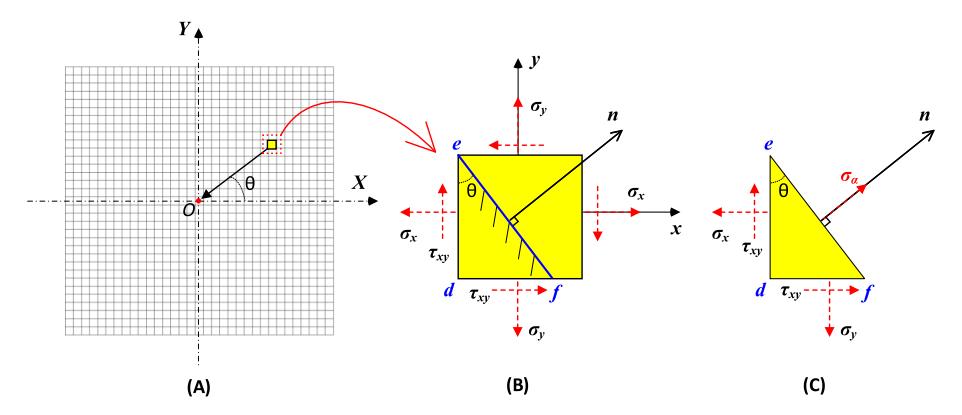


Fig. 5. Schematic diagram of the decomposition of pore pressure in a single unit towards the centre of the cross-section. (A) Global model, (B) Local model for each unit, and (C) Force decomposition for each unit. "O" is the centre of the global model. "X" and "Y" are the x- and y-axis of the global model. "x" and "y" are the x- and y-axis of the local model. "\textit{\textit{G}"} is the angle of pore pressure for each unit to the positive direction of global X-axis. "\textit{\textit{e}}" is the inclined section of a single unit.

conditions were applied by constraining the central element of the crosssection in both the x and y directions to prevent the overall translational motion (i.e., rigid body motion). Proper constraints were essential in finite element analysis of deformable bodies, as failing to address rigid body motion can result in non-unique solutions or numerical instability. For force boundary conditions, the pore pressure time history, derived from the water content distribution, was applied to the mechanical model. The same topological information, including geometry and meshing, was used consistently across the mechanical and water transport models. The pore pressure applied to each element varied spatially and was determined based on its relative orientation to the centre of the model. The elastic modulus and Poisson's ratio of pastes with different silicate moduli were considered as 14 Gpa and 0.2 [32], respectively. These properties remained constant during 1 h of water immersion. Additionally, the deformation of the cross-section of the paste of m = 1.5was specifically calculated to show the cracking mechanism more intuitively. It should be noted that the mechanical model did not account for internal stress redistribution caused by cracking.

#### 3. Experimental results

#### 3.1. Strength

Fig. 6A shows the flexural strength of 7 d AAS pastes under sealed and water-immersed conditions. Under sealed conditions, the flexural strength of all four pastes increased with time while did not show an increasing trend with the increase of silicate moduli. In principle, an activator with a higher silicate modulus contains a higher content of soluble Si, which, in turn, promotes the formation of gels and the densification of microstructure [11]. This densification is theoretically associated with higher flexural strength. However, the finer microstructure resulting from higher silicate moduli also generates significant pore pressure from unsaturated menisci, leading to high internal stress and shrinkage [34]. Consequently, microcracks were frequently observed on the surface of AAS pastes with high silicate moduli. As the flexural strength was sensitive to microcracks, the flexural strengths of m = 1 and m = 1.5 were lower than those of m = 0.5 at the same ages. Additionally, the paste of m = 0 showed the lowest flexural strength among the four groups, attributed to its relatively porous microstructure.

The flexural strength of samples subjected to water immersion showed different trends compared to those under sealed conditions. The flexural strength of the m=0 under "7 s + 7w" was higher than that under "7 s + 7 s", while the flexural strength of the other three prisms decreased to different extents upon immersion as the silicate modulus increased. This was because water ingress into the relatively porous  $m=0\,$  paste can mitigate the shrinkage, reducing internal stress and

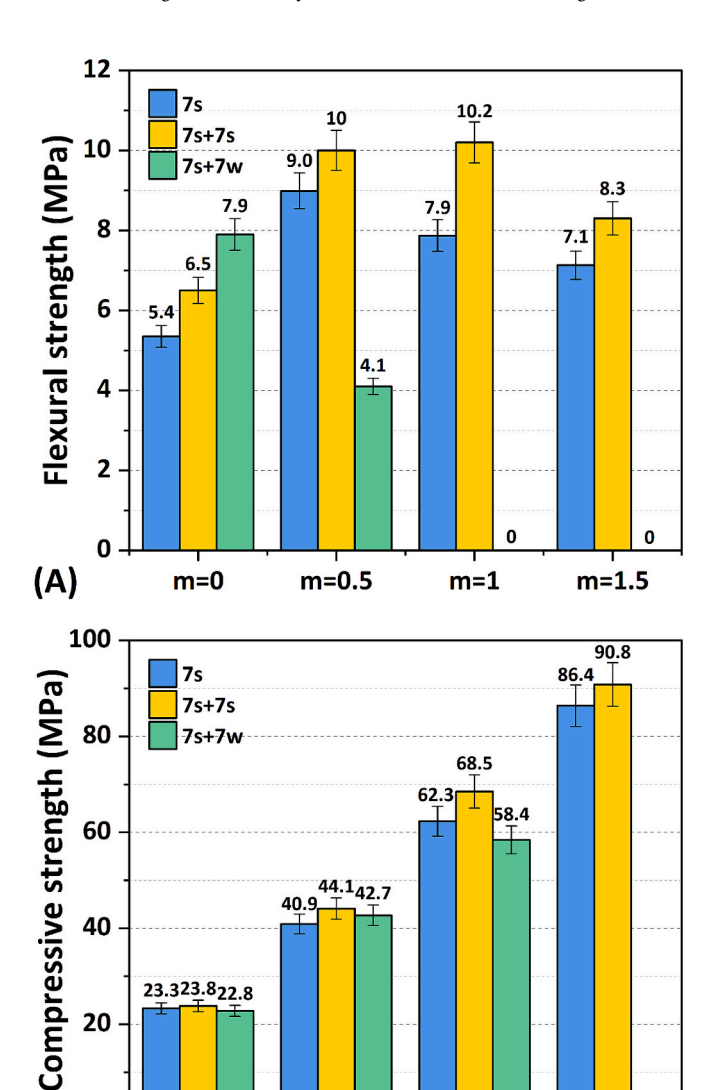


**Fig. 6.** Flexural (A) and compressive strength (B) of AAS pastes under sealed and water-immersed conditions. The "7s" indicates 7 d of sealed curing while the "7w" refers to 7 d of water immersion.

m=1

m = 0.5

0

m = 1.5

0

m=0

(B)

minimizing the development of microcracking. As a result, water immersion was conducive to the flexural strength development of pastes with a low silicate modulus at early ages. However, the paste with m = 1was broken into sections and the paste with m = 1.5 was completely fragmented after 19 h of water immersion, as shown in Fig. 7. Both of these two pastes showed no measurable flexural strength after immersion. It was evident that water immersion adversely affects the development of flexural strength in sodium silicate-based AAS pastes. This was consistent with the findings from previous works [11,16,19,35]. Furthermore, it was interesting to observe that the m = 1.5 prisms were not only broken into several sections like the m=1 prisms but even into pieces, especially at the corners of prisms (highlighted in dashed red circles in Fig. 7). Similar observations were also shown in [18]. This phenomenon indicated severe structural problems of AAS pastes under immersed conditions, which has been scarcely reported in previous research and warranted significant attention.

Fig. 6B shows the compressive strength of AAS pastes under sealed and water-immersed conditions. Unlike flexural strength, the compressive strength of AAS pastes under sealed conditions increased with both ages and silicate moduli. This was because the compressive strength is more dependent on the porosity of the microstructure instead of microcracks. Additionally, the sample after water immersion only showed a slightly lower value than that under sealed conditions at the same age. This indicated that 7 d of water immersion does not significantly affect the pore structure of the matrix, although the leaching of alkali ions may dilute the pore solution and impede the reaction of slag [11]. Due to the complete breaking of the prismatic samples, the compressive strength of  $m=1.5\ prisms$  after immersion was zero.

#### 3.2. Phase assemblage

Fig. 8 shows the XRD pattern of piece AAS pastes with different silicate moduli under "7s", "7s + 7s" and "7s + 7w" curing conditions. Generally, gels and hydrotalcite were the two main reaction products in an AAS paste [36,37]. It was observed that the characteristic peaks of gels in pastes with a low silicate modulus were more pronounced than those with a high silicate modulus. In particular, the peaks, marked with an asterisk symbol "\*", were exclusively observed in the m=0 paste. This was because the gel in a high-modulus paste normally shows a low

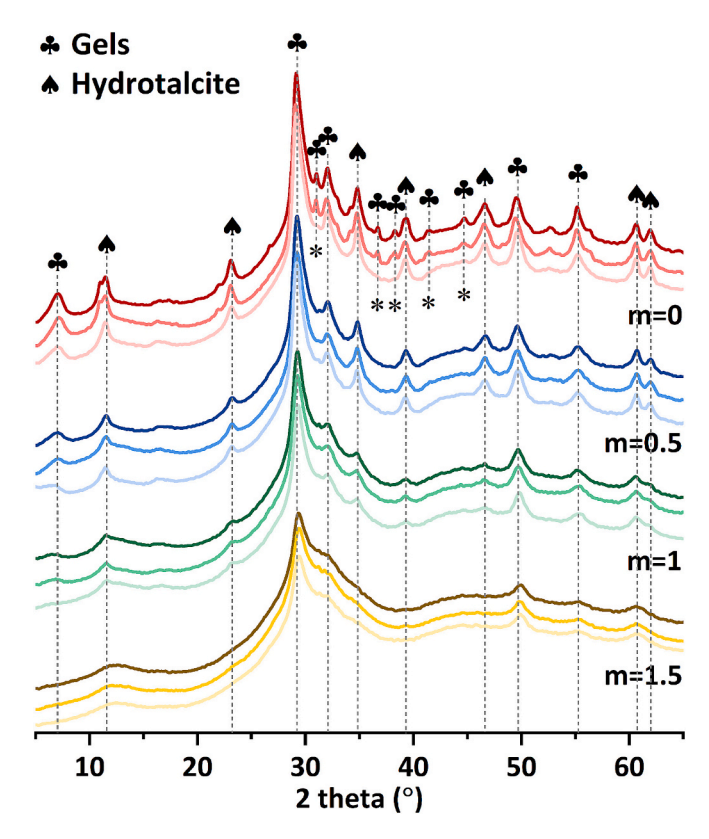


**Fig. 8.** XRD pattern of AAS pastes with different silicate moduli under sealed and water-immersed conditions. The curves with colours from dark to shallow in each group represent the sample of "7s", "7s + 7s" and "7s + 7w", respectively. The "\*" marks the characteristic peak of gels only existing in the m=0 paste. (For interpretation of the references to colour in this figure legend, the reader is referred to the web version of this article.)

Ca/Si ratio, resulting in a more crosslinked and amorphous structure, which obscured the reflections of some representative crystal planes in the Si-Al tetrahedra. Additionally, the characteristic peaks of hydrotalcite diminished with the increase of silicate modulus, indicating that a



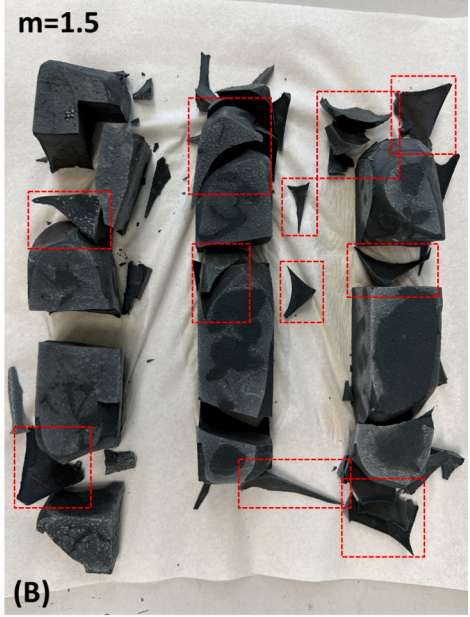


Fig. 7. Fracture of the AAS prismatic pastes with m = 1 and m = 1.5 after 19 h of water immersion. The photo was taken immediately after the samples were removed from water, without undergoing the drying process.

high silicate content hindered the formation of crystalline hydrotalcite.

In the comparison of sealed and water-immersed samples, the phase assemblage of pastes remained stable and only the peaks of gels, marked as the asterisk symbol "\*" in the m=0 paste became less evident after 7 d of water immersion. This implied, in part, the decomposition of some chemical units in gels upon exposure. Since no secondary phases were identified in the paste after 7 d of immersion, the expansion of some crystals can be excluded as a possible reason for the cracking.

#### 3.3. Paste chemistry

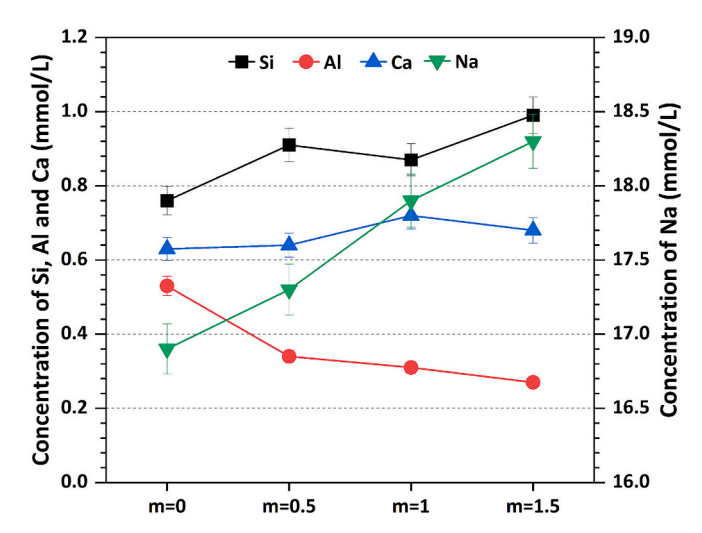
Fig. 9A shows a representative BSE image of AAS pastes with m=1 at 7 d, which typically contains unreacted slag, inner products, outer products and pores. The inner products, identifiable as the dark rim of slag, were predominantly composed of hydrotalcite-like phases, along with C-(N-)A-S-H gels [38]. Due to the dissolution and diffusion of Ca and Si species from slag, the greyscale of the rim was usually higher than slag particles [38,39]. In contrast, the outer products consist exclusively of C-(N-)A-S-H gels due to the limited mobility of Mg [39,40]. Therefore, to better understand the chemical composition of gels, we selected the outer product as the detecting region for point analysis.

Fig. 9B shows the atomic ratio of Ca/Si versus Na/Si in the outer product of AAS pastes. A negative correlation was observed between the Ca/Si and Na/Si ratios, probably due to a competitive relationship between Ca and Na in the role of charge balance [41]. The gel in the paste with a higher modulus showed a lower Ca/Si ratio and a higher Na/Si ratio. This can be ascribed to the presence of soluble Si in the sodium silicate-based activators, which can supply additional Si for a direct reaction with dissolved Ca and Al from slag to the formation of gels. Due to the substantial formation of gels, free Na<sup>+</sup> ions present in the pore solution assume the responsibility for charge balance. Consequently, this resulted in a heightened Na/Si ratio of gels in the outer products of the m=1 and m=1.5 pastes. As reported in [42], the bulk modulus of gels was partly determined by the interlayer density. Elevated content of interlayer Ca can yield higher bulk stress at a comparable basal spacing. In other words, the gel with a higher Ca/Si ratio showed a superior intrinsic mechanical property. It can be inferred that the C-(N-)A-S-H gels in the m=1.5 and m=1 pastes exhibited weaker mechanical properties than those in the m=0.5 and m=0 pastes. This could be a contributing factor to the significant cracking phenomenon observed in the m = 1.5 paste.

#### 3.4. Leaching behaviour

The leaching behaviour can reflect the thermodynamic stability of AAS pastes subjected to water immersion. Considering the minimal dissolution loss of slag and hydrotalcite in deionized water [11], the ions leached into the solution can be mainly attributed to the decomposition of C-(N-)A-S-H gels. Fig. 10 shows the ion concentrations of Si, Al, Ca and Na in the leachate of AAS powdered samples after 7 d of water immersion. The ion concentrations of Si and Ca in the four leachates were comparable, and the paste with a higher silicate modulus generally showed a higher value. Si and Ca are the two main elements in the gel structure, and their leaching is detrimental to the stability of gels [43]. This indicated that the gels in the pastes with high silicate moduli were more vulnerable to leaching.

Furthermore, it was observed that Al in the leachate of the paste with a higher silicate modulus had a lower concentration, probably due to a lower content of Al in the paste with a higher silicate modulus. A higher content of sodium silicate in the activator results in a lower pH at the same dosage of Na, which would impede the decomposition of slag and the dissolution of Al. Additionally, it was evident that the leached ions were predominantly composed of Na, as an indicator of its weak bond with gels and high mobility in aqueous conditions [43,44]. The



**Fig. 10.** Ion concentration of Si, Al, Ca (on the left Y) and Na (on the right Y) in the leachate of AAS powdered samples after 7 d of water immersion.

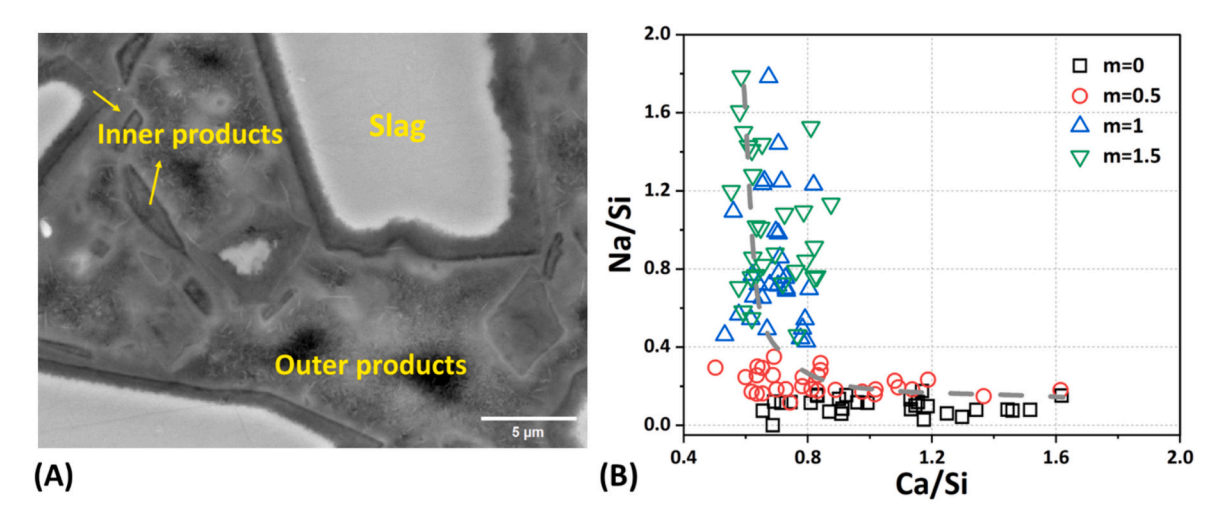


Fig. 9. (A) A representative BSE image of AAS paste with m = 1 sealed for 7 d; (B) Atomic ratios of Ca/Si against Na/Si in the outer products of 7 d sealed AAS pastes with different silicate moduli.

concentration of Na in the leachate of the paste with a higher silicate modulus exhibited a higher Na/Si ratio in gels (Fig. 9B). This was consistent with the dissolution of synthetic C-(N-)A-S-H gels [53], in which the gel with a lower Ca/Si ratio showed a higher leaching amount of Na. Moreover, as reported in [43], the leaching of Na in the interlayer can trigger the migration of intralayer Ca to the interlayer for charge compensation. This subsequently resulted in the decalcification of the intralayer and the formation of a more crosslinked gel structure. Therefore, this considerable leaching of Na in the paste of  $m=1.5\ could$  suggest a substantial change in its gel structure. To further understand the structural change of gels induced by leaching, FTIR tests were performed.

#### 3.5. Gel stability

The infrared spectra of AAS pastes are depicted in Fig. 11. As demonstrated in Fig. 11A, the most pronounced peak is situated at around 950 cm<sup>-1</sup>, which corresponds to the asymmetrical stretching vibration of Si-O-Si or Si-O-Al in Q<sup>2</sup> units. In the low-frequency range of this main peak, a small shoulder is noticeable at 890 cm<sup>-1</sup>, which is assigned to the bending vibration of Si-O [45]. Notably, the paste with a higher silicate modulus exhibited a less pronounced absorption peak compared to that with a lower modulus, particularly near 890 cm<sup>-1</sup>. This finding matched with the XRD results and indicated that the gel in high-modulus pastes was comparatively less ordered and the characteristic chemical group remained less evident. In the comparison of pastes before and after exposure, 7 d of water exposure had a limited impact on the main gel structure, which was consistent with [11,43]. However, there were subtle variations with regard to the wavenumber of Q<sup>2</sup> units.

Fig. 11B shows the peak value of the  $Q^2$  unit in the four AAS pastes before and after water immersion. Typically, a higher wavenumber of the  $Q^2$  peak indicates a higher degree of polymerization of gels. The wavenumber of the  $Q^2$  peak increased with the increase of silicate moduli, which suggested that the gel in the high-modulus paste had a more crosslinked structure [46]. As shown in Fig. 9B, the gel in the pastes of m=1 and m=1.5 shows a lower Ca/Si ratio, which implies a reduced content of Ca in the Ca-O of the intralayer. A lower content of Ca

in the intralayer is conducive to a prolonged silicate chain. In contrast to the sealed AAS pastes, the gel in pastes after water immersion showed a higher wavenumber, indicating a higher polymerization degree. As discussed above, this was mainly due to the leaching of Na. Moreover, it was also observed that the growth of the wavenumber of the  $\mathbf{Q}^2$  unit in m=1 and m=1.5 pastes upon exposure was more pronounced than that of m=0 and m=0.5 pastes. This discrepancy can be ascribed to the variation in Na leaching across different systems (Fig. 10). A greater loss of interlayer Na corresponds to a more significant structural evolution. Among these four pastes, the gel in the m=1.5 paste showed the highest Na loss and thereby underwent the most severe structural change when subjected to water exposure. This structural evolution of gels can promote the development of microcracks, which is harmful to the underwater stability of the materials.

#### 3.6. Pore structure

Fig. 12 shows the cumulative mercury intrusion and pore size distribution of 7 d AAS pastes. It was observed that the open porosity of pastes decreased from 26.5% to 7.9% as the silicate modulus increased from 0 to 1.5. This indicated that the presence of soluble Si in initial activators can effectively densify the microstructure. The effective porosity, referring to the ratio of interconnected pores allowing fluid flow, in the paste with a higher silicate modulus, also showed a lower value and decreased with an increase in modulus. This implied that a high-modulus paste has low water permeability.

Moreover, the threshold pore diameter of the pastes diminished from 36.25 nm to 2.63 nm as the silicate modulus increased from 0 to 1.5. The threshold pore diameter is defined as the pore diameter with the highest rate of mercury intrusion per change in pressure or diameter (dV/dP or dV/dD) [47]. Powers et al. [48] found that the permeability of cement pastes dramatically decreases when the pore threshold falls below a critical value. In such a scenario, water penetrated through the gel pore, typically within the range of 1–10 nm, which was over an order of magnitude smaller than the capillary pore (10 nm-100  $\mu$ m) [49]. Therefore, the water flow in the m = 1 and m = 1.5 pastes would be considerably lower than that in the m = 0 and m = 0.5 pastes, since the

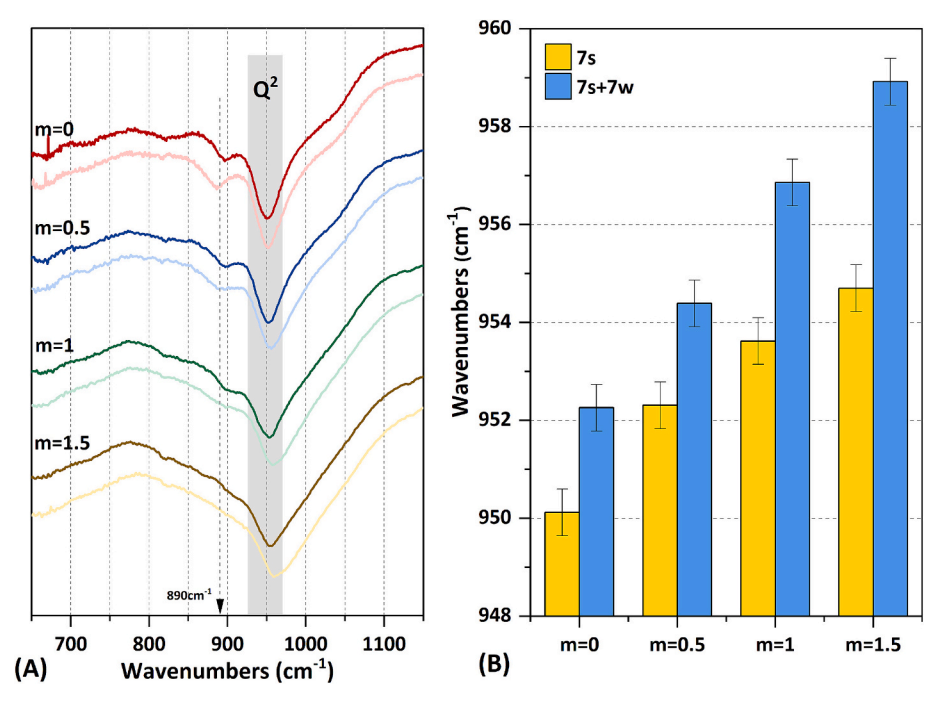


Fig. 11. (A) FTIR pattern of powdered 7 d AAS pastes before and after 7 d of water immersion. The curves in dark and light colours represent the sample with and without exposure, respectively. (B) The peak value of wavenumbers of the  $Q^2$  units in gels of different AAS pastes. (For interpretation of the references to colour in this figure legend, the reader is referred to the web version of this article.)

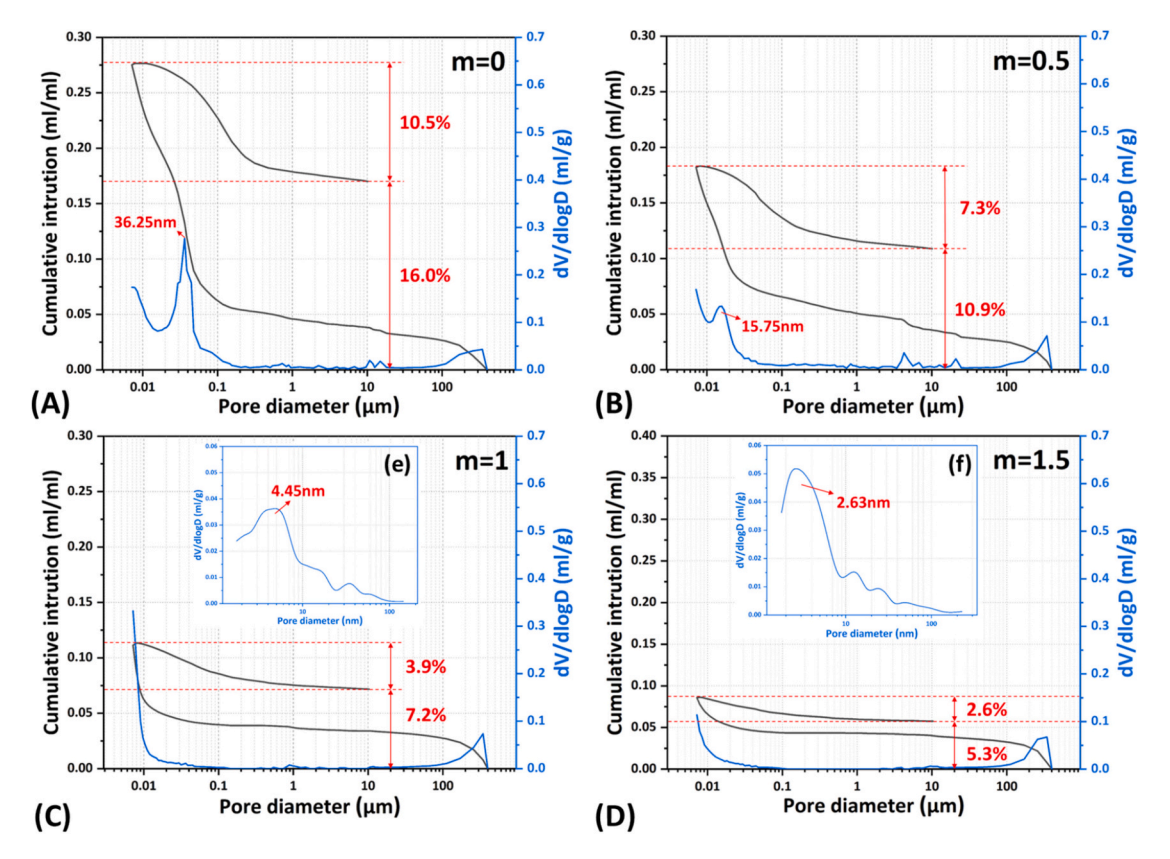


Fig. 12. Pore structure information of AAS pastes obtained from MIP test (A–D) and N<sub>2</sub> absorption test ((e) and (f)) results. The percentages in each inset indicate the effective porosity and ink-bottle porosity.

flow in the former two systems was contained by gel pores while that in the latter ones was controlled by small capillary pores. The distinct pore structures in different pastes would result in different behaviours of water transport.

#### 4. Simulation results

### 4.1. Distribution of saturation degree and pore pressure in AAS materials underwater

With the reaction of slag in AAS pastes, the water content in the pore structure gradually decreases. Due to the capillary suction, water is allowed to be absorbed into part of the unsaturated pores when the material is immersed. The absorption of water initiates from the surface part of the sample, resulting in uneven distribution of water content in the material. Given the typically rapid process of capillary suction and the time-consuming measurements of CT scans, we thereby used FEM to simulate this phenomenon in different porous media. The distribution of the saturation degree of the cross-section of four pastes with time is shown in Appendix A Fig. S2. The distribution of the saturation degree of the cross-section of AAS prisms subjected to water immersion at 1 h is shown in Fig. 13. After 1 h of exposure, the pastes of m = 0 and m = 0.5had become nearly saturated (Fig. 13A and B), indicated by a higher saturation degree in the central part compared to the initial state. However, water seemed to have failed to permeate into the pastes of m = 1 and m = 1.5 due to their low permeabilities, which led to an uneven distribution of water content in the material. The distribution of saturation degree is crucial for the structural stability of the matrix, as it can further impact the distribution of pore pressure.

Fig. 14 shows the pore pressure distribution of the cross-section of AAS prisms subjected to water immersion at 1 h. It was observed that the magnitude of pore pressure in matrices with different silicate moduli varies considerably, primarily attributed to the discrepancy in the pore

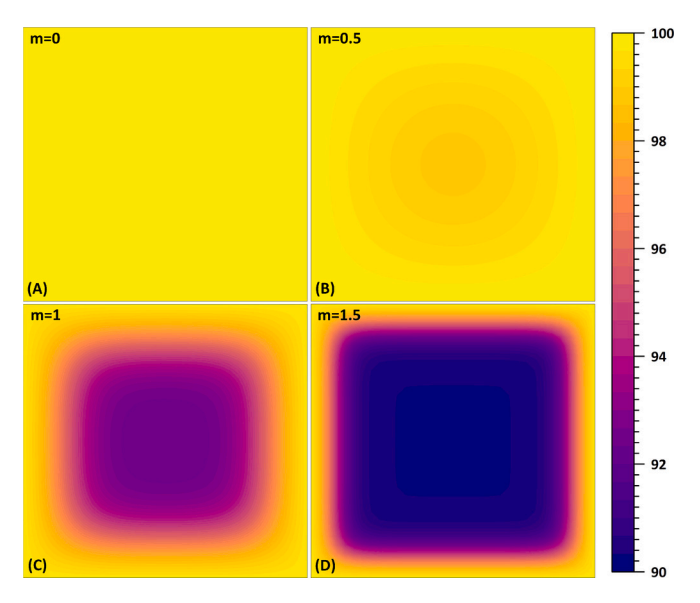


**Fig. 13.** Distribution of the saturation degree (unit: %) of the cross-section (4 cm  $\times$  4 cm) of AAS prisms at 1 h of water immersion. The saturation degrees of 7 d pastes of m = 0, 0.5, 1 and 1.5 before water immersion were measured as 94.6%, 93.8%, 92.3% and 90.2%, respectively.

pressure before exposure to water. According to Eq. (6), the pore pressure depends on the saturation degree  $(\theta/\phi)$  of the material. The additional soluble Si from activators promotes the formation of gels, which can consume more water and lower the water content in the system. Therefore, the paste with a higher silicate modulus showed a lower saturation degree and thus a higher pore pressure.

Interestingly, the pattern of pore pressure appeared to resemble that

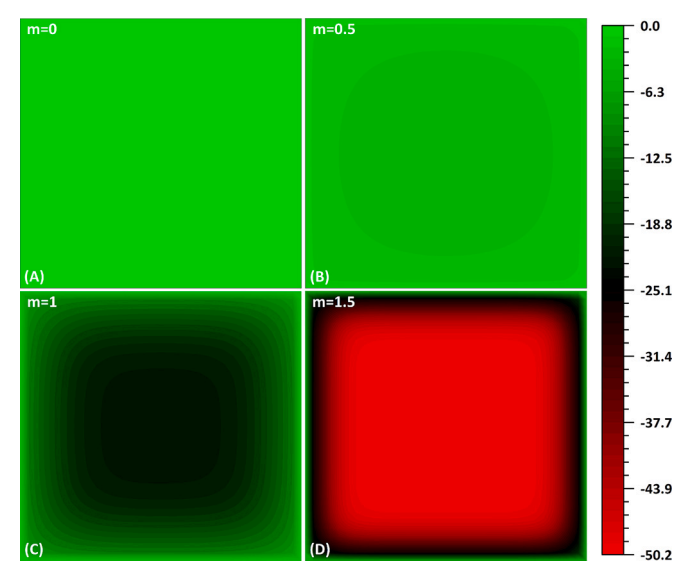


**Fig. 14.** Distribution of the pore pressure (unit: MPa) of the cross-section (4 cm  $\times$  4 cm) of AAS prisms at 1 h of water immersion. The pore pressure of the centre (the highest part) of the four materials is -0.87 MPa, -3.9 MPa, -22.65 MPa and -50.2 MPa, respectively.

of the saturation degree, as an indicator of a correlation between them. With the penetration of water, the outer part became percolated, and the saturation degree increased over time. Due to the negative relationship between saturation degree and pore pressure (Eq. (6)), the percolated part showed lower pore pressure than the relatively dry part, thereby resulting in the existence of a gradient of pore pressure. Furthermore, the gradient of pore pressure in the paste with a higher silicate modulus was steeper. On one hand, pastes in the presence of high Si were denser and more resistant to water intrusion. This resulted in a thinner depth of the affected area in m=1 and m=1.5 compared to m=0 and m=0.5. On the other hand, the initial pore pressure of high-modulus pastes was much higher than that of low-modulus ones. This gradient of pore pressure would eventually lead to the rearrangement of internal stress.

## 4.2. Distribution of principal tensile stress and deformation in AAS materials underwater

The obtained distribution of pore pressure was subsequently transferred to the distribution of internal tensile stress. During the calculation process, it was found that the distribution of internal tensile stress matched the cracking observed in the paste of m = 1.5 when the static equilibrium process reached about 90% completeness. This was probably because this model did not account for the deterioration of mechanical properties and structural failure of materials during water immersion. For consistency, the distribution of the principal tensile stress across the cross-section of four AAS prisms was studied at the completeness of 90%. Fig. 15 shows the distribution of the principal tensile stress in the cross-section of AAS pastes at 1 h of water immersion. To better evaluate the cracking potential of different pastes, the flexural strength of four AAS pastes at 7 d (m=0: 5.4 MPa, m=0.5: 9.0 MPa, m = 1:7.9 MPa and m = 1.5:7.1 MPa) was set as the threshold. It is important to note that flexural strength is normally higher than tensile strength [50,51]. In other words, if the simulated tensile stress of a local region exceeds the measured flexural strength, it must surpass the tensile stress of the material, indicating a high cracking potential.

Consistent with the result of pore pressure, the paste with a higher silicate modulus underwent higher internal stress on average. It was observed that both the magnitude and the gradient of tensile stress were low in the pastes of m=0 and m=0.5 (Fig. 15A and B). This indicated a low risk of cracking in pastes with low silicate moduli. However, for

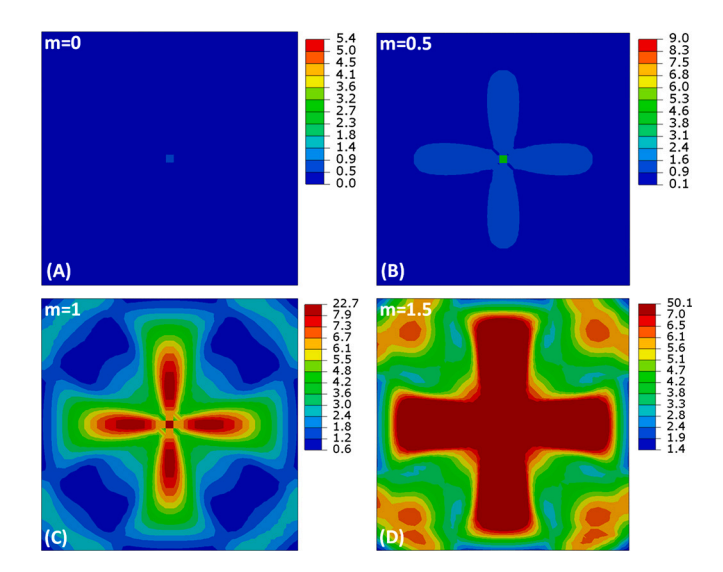
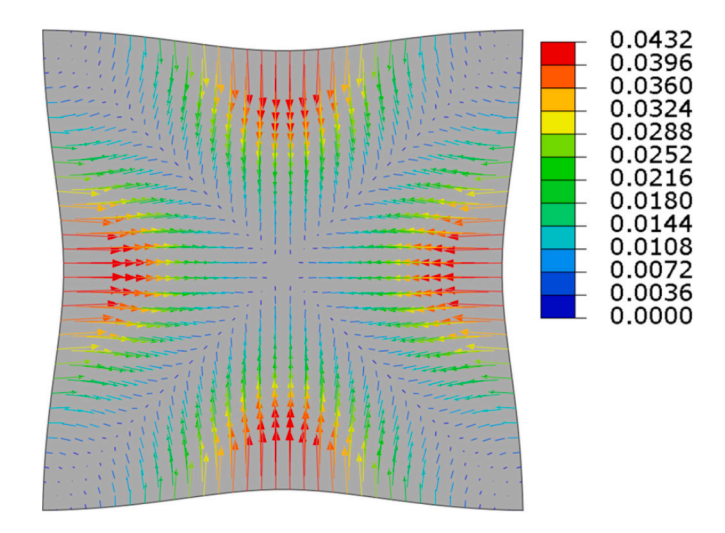


Fig. 15. Distribution of the principal tensile stress (unit: MPa) in the cross-section (4 cm  $\times$  4 cm) of AAS prisms at 1 h of water immersion. In comparison with the results of flexural strength, the red and crimson regions indicate the areas with high cracking potential. (For interpretation of the references to colour in this figure legend, the reader is referred to the web version of this article.)

pastes with m=1 and m=1.5, regions with stress concentration were observed at the centre and corners of the section. More specifically, the tensile stress of a cross-like region located at the centre of the m=1 paste was higher than 7.9 MPa (Fig. 15C), indicating a fracture potential in the centre of the prism. This was consistent with the observation in Fig. 7A, where the prisms of m=1 were broken into halves after water immersion. However, not only the centre but also the corners of the section experienced high tensile stress (approaching the threshold of 7.1 Mpa) in the sample of m=1.5 (Fig. 15D). This suggested a high cracking potential at the corner of the section. As presented in Fig. 7B, the spalling of samples at the corners was evidently visible, which corresponded to the simulated results when viewed in three dimensions.

For a more direct understanding of this issue, the deformation in the



**Fig. 16.** Deformation (unit: mm) of the cross-section (4 cm  $\times$  4 cm) of the AAS prisms with m = 1.5 at 1 h of water immersion, amplified 40 times. The value is calculated based on the distribution of internal stress, with the elastic modulus and Poisson's ratio of the m = 1.5 paste at 7 d (under sealed conditions) set as 14 GPa and 0.2, respectively [32]. Please note that the deformation is magnified in the visualization, while the value on the labels represents the actual deformation in millimetres.

section of the m = 1.5 paste was amplified 40 times, as shown in Fig. 16. By and large, the deformation of the side of the section was larger than that of the corner and the diagonal, which led to uncoordinated deformation in the plane and thus the spalling of corners. It should be noted that the mechanical model did not account for internal stress redistribution caused by cracking. In reality, cracking alleviates tensile strength in stress concentration regions, but introduces new stress concentrations at the crack tips. This process is highly complex and challenging to incorporate in each iterative step. Instead, the simplified model used high tensile stress as an indicator of cracking potential, aligning with experimental observations of crack distribution. This simplification was effective in understanding the underlying mechanisms behind the cracking problems, which can also reduce computational cost and enhance its feasibility for engineering applications. Future research is expected to incorporate plastic damage evolution and evaluate the impact of aggregate on stress distribution. Such advancements will offer more precise guidance for designing AAMs under aqueous conditions.

#### 5. Discussion

#### 5.1. Cracking mechanisms of AAS materials underwater

#### 5.1.1. Chemical perspective

Although no expansive reaction product formed and no evident phase decomposition was identified in AAS pastes after short-term water immersion, the C-(N-)A-S-H gels can undergo structural evolution. This structural change is dependent on the chemical composition and leaching loss of gels. With the increase of silicate modulus, the content of

Si in the gels increases, resulting in a lower Ca/Si ratio and a higher Na/Si ratio. These gels not only are more amorphous but also exhibit lower intrinsic mechanical properties [42]. More importantly, gels in the paste with high silicate moduli lose more Na when exposed to water immersion, leading to more severe structural changes. It is plausible that the cracking propagation in the paste with high silicate moduli is more likely to happen since the gels experience more significant structural changes underwater.

#### 5.1.2. Physical perspective

Due to the capillary suction of unsaturated pores, water can penetrate the matrix of AAS prisms. This process can increase the water content and lower the pore pressure of percolated pastes. However, the unwetted part still shows low water content and high pore pressure, which eventually leads to the gradient of pore pressure and uneven distribution of internal stress. At a low silicate modulus (m=0 and m=00.5), the matrix was relatively permeable, allowing water to penetrate easily. This resulted in a low gradient of pore pressure and low internal stress. No cracking potential was found in both the experimental and computational results. However, at a high silicate modulus, the microstructure of pastes became dense, and the depth of water penetration decreased. The discrepancy in water content between the external and internal parts caused a steep gradient of internal stress. Simulation results showed that the tensile stress at the centre of the prism of m=1exceeded its flexural strength, which indicated a potential for cracking or fracture in the middle of the samples. This was consistent with the experimental observation. As the silicate modulus increased to 1.5, the cracking problem was exacerbated. The prism of 1.5 not only fractured

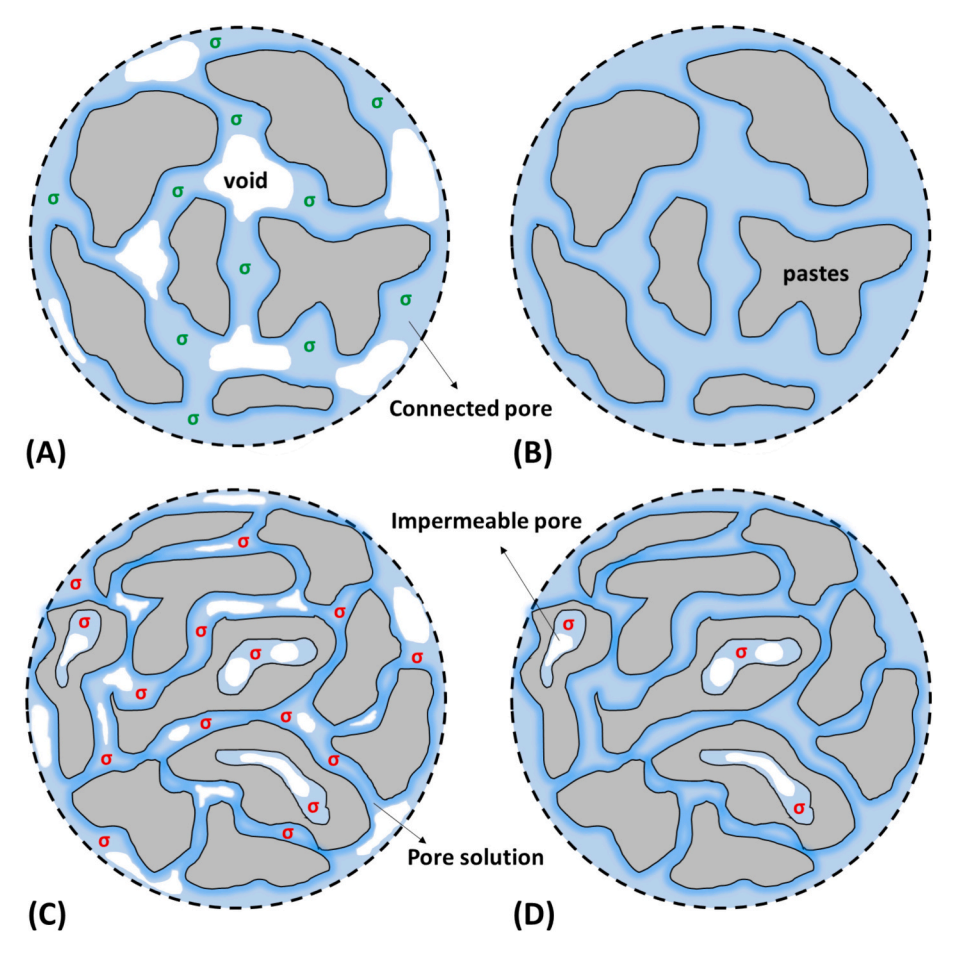


Fig. 17. Representation diagrams of AAS pastes with low (A and B) and high porosity (C and D) before and after water percolation. The unreacted slag and reaction products are omitted in the paste. The pore pressure of  $\sigma$  in red is higher than the one in green due to the smaller radius of the menisci. (For interpretation of the references to colour in this figure legend, the reader is referred to the web version of this article.)

into several sections but also showed corner spalling. This was attributed to the high tensile stress at the corner of the prism exceeding the limit of the material.

To simplify the modelling process, it was assumed that the pores in the media were connected and the porous media can be entirely percolated over a sufficient period. However, in a real AAS paste, the pores may not be fully connected, especially with a high silicate modulus ratio. This results in the presence of some small capillary pores or gel pores that are impermeable, even though external water has intruded the nearby region. Fig. 17 depicts representation diagrams of AAS pastes with low and high porosity before and after percolation. In the case of the paste with low silicate moduli, the material is porous and the pores are interconnected (Fig. 17A). After water ingress, the pores on the surface of the material become saturated and the pore pressure can decrease to almost zero (Fig. 17B). However, in pastes with high silicate moduli, the material is dense and some pores are impermeable (Fig. 17C). After the ingress of water, these pores remain unsaturated with high pore pressure (Fig. 17D). Additionally, as indicated by flexural strength results (Fig. 6A), some microcracks might exist in the sealed pastes with high silicate moduli. If the residue stress in the impermeable pore exceeds the limit of the paste, it will promote microcrack propagation. This could serve as another explanation for why the paste with m = 1.5 fractures into pieces after water immersion.

#### 5.2. Potential mitigation strategies

Based on the cracking mechanisms, some potential strategies can be proposed to mitigate this problem. From the chemical perspective, increasing the Ca/Si ratio of C-(N-)A-S-H gels is essential to reduce Na leaching and limit the structural evolution of gels. For plain slag systems, reducing the silicate modulus can effectively decrease the content of Si, thereby increasing the Ca/Si ratio in gels. For slag blended systems, increasing the dosage of slag can elevate the Ca/Si ratio of C-(N-)A-S-H gels. From the physical perspective, while denser matrices may improve mechanical properties under sealed conditions, they are not necessarily ideal for mitigating cracking problems caused by water immersion. Moderate dosages of sodium silicate and slag can result in a matrix with sufficient permeability to reduce stress gradients while avoiding overly dense or highly porous structures. Incorporating relatively inert aluminosilicate precursors, such as fly ash or metakaolin, can moderate reaction rates and coarsen the microstructure. This enhances the ability of materials to accommodate water transport without excessive stress buildup.

Additionally, the addition of fine aggregate can partially address this problem. Given that flexural strength is highly sensitive to cracks, it serves as a reasonable indicator for evaluating cracking problems. In this study, we also measured the flexural strength of AAS mortars with different silicate moduli (Appendix A Fig. S5) as well as in our previous work [52]. Here, the flexural strength of m = 1.5 mortars subjected to water immersion was measurable but lower than those under sealed conditions. This indicated that cracking problems persisted in mortars, even though they were less evident than in pastes. In our previous work [52], the m = 1 mortar showed a decreasing flexural strength trend under high-humidity conditions with time, while showing an increasing trend under ambient and sealed conditions. These findings suggested that while the addition of aggregates mitigated cracking to some extent, it did not completely eliminate this problem. The optimal solution lies in refining the mixture design, considering both the paste chemistry and pore structure. In terms of experimental and computational results, a silicate modulus of no higher than 0.5 is recommended for plain AAS materials.

#### 6. Conclusions

In this study, the behaviour of AAS pastes with varying silicate moduli subjected to water immersion was investigated. We found that the pastes with high silicate moduli exhibited cracking and, in some cases, fragmentation under these conditions. The underlying mechanisms of these phenomena were elucidated chemically and physically. Based on the experimental and simulation results, some conclusions can be drawn as follows:

- 1. Apart from the prism of m=0, the flexural strength of the other three AAS prisms ( $m=0.5,\ m=1$  and m=1.5) decreased to varying extents after 7 d of water immersion. Notably, the prisms with m=1 fractured into halves, while those with m=1.5 were fragmented, resulting in no measurable flexural strength. However, other than the prism with m=1.5, AAS pastes exhibited minimal adverse effects from water immersion in terms of compressive strength.
- 2. The phase assemblage of all four AAS pastes before and after 7 d of water immersion was comparable, with no formation of new crystals observed. The C-(N-)A-S-H gel in the paste with a higher silicate modulus showed a higher leaching loss of Na, due to an initially higher Na/Si ratio. The heightened leaching of Na can trigger more severe structural change and deterioration of gels, which potentially contributed to crack propagation.
- 3. The simulated results indicated that pastes with m=1 and m=1.5 showed lower permeability and higher pore pressure than those with m=0 and m=0.5. This led to a steeper gradient of pore pressure and higher internal stress within the matrix with high silicate moduli. According to the simulation results, stress concentration was observed at the centre and corners of the cross-section in the paste with m=1.5, exceeding the flexural strength of the material. These findings were consistent with experimental observation, where fractures occurred at the centre and spalling was evident at the corners of prisms.
- 4. Considering both chemical and physical perspectives, a low silicate modulus (no higher than 0.5) was recommended to address the cracking issue of AAS materials underwater. In such a system, the C-(N-)A-S-H gel showed fewer structural changes and the matrix shows lower internal tensile stress subjected to water immersion.

#### CRediT authorship contribution statement

**Chen Liu:** Writing – original draft, Methodology, Investigation, Conceptualization. **Jinbao Xie:** Methodology, Investigation. **Zhenming Li:** Writing – review & editing, Supervision. **Guang Ye:** Writing – review & editing, Supervision, Project administration.

#### Declaration of competing interest

The authors declare that they have no known competing financial interests or personal relationships that could have appeared to influence the work reported in this paper.

#### Acknowledgement

Chen Liu would like to acknowledge the funding supported by the China Scholarship Council (CSC) under grant No. 201906950102. Zhenming Li would like to acknowledge the Guangdong Provincial Key Laboratory of Intelligent and Resilient Structures for Civil Engineering (2023B1212010004).

#### Appendix A. Supplementary data

Supplementary data to this article can be found online at https://doi.org/10.1016/j.cemconres.2025.107877.

#### Data availability

Data will be made available on request.

#### References

- [1] A. Vollpracht, B. Lothenbach, R. Snellings, J. Haufe, The pore solution of blended cements: a review, Mater. Struct. Constr. 49 (2016) 3341–3367, https://doi.org/ 10.1617/s11527-015-0724-1.
- [2] K. Natkunarajah, K. Masilamani, S. Maheswaran, B. Lothenbach, D.A. S. Amarasinghe, D. Attygalle, Analysis of the trend of pH changes of concrete pore solution during the hydration by various analytical methods, Cem. Concr. Res. 156 (2022) 106780, https://doi.org/10.1016/j.cemconres.2022.106780.
- [3] P. Faucon, F. Adenot, R. Cabrillac, M. Jorda, Deterioration mechanisms of a cement paste under water attack, Concr. under Sev. Cond. 2 (1998) 123–132.
- [4] K. Haga, S. Sutou, M. Hironaga, S. Tanaka, S. Nagasaki, Effects of porosity on leaching of Ca from hardened ordinary Portland cement paste, Cem. Concr. Res. 35 (2005) 1764–1775, https://doi.org/10.1016/j.cemconres.2004.06.034.
- [5] J. Jain, N. Neithalath, Analysis of calcium leaching behavior of plain and modified cement pastes in pure water, Cem. Concr. Compos. 31 (2009) 176–185, https:// doi.org/10.1016/j.cemconcomp.2009.01.003.
- [6] M. Luo, Q. Zeng, X. Pang, K. Li, Effect of curing conditions on pore structure of cement based materials, J. Chin. Ceram. Soc. 41 (2013) 597–604.
- [7] J.L. Provis, A. Palomo, C. Shi, Advances in understanding alkali-activated materials, Cem. Concr. Res. 78 (2015) 110–125, https://doi.org/10.1016/j. cemconres.2015.04.013.
- [8] J.L. Provis, Alkali-activated materials, Cem. Concr. Res. 114 (2018) 40–48, https://doi.org/10.1016/j.cemconres.2017.02.009.
- [9] L. Feng, S. Yi, S. Zhao, Q. Zhong, F. Ren, C. Liu, Y. Zhang, W. Wang, N. Xie, Z. Li, N. Cui, Recycling of aluminosilicate-based solid wastes through alkali-activation: preparation, characterization, and challenges, Buildings 14 (2024), https://doi. org/10.3390/buildings14010226.
- [10] S.S. Rathore, C.R. Meesala, Influence of recycled coarse aggregate on properties of fly ash and slag-based geopolymer concrete cured under oven and ambient temperature, World J. Eng. (2024), https://doi.org/10.1108/WJE-12-2023-0524.
- [11] C. Liu, X. Liang, Y. Chen, Z. Li, G. Ye, Degradation of alkali-activated slag subject to water immersion, Cem. Concr. Compos. 142 (2022), https://doi.org/10.1016/j. cemconcomp.2023.105157.
- [12] G. Huang, Y. Ji, L. Zhang, J. Li, Z. Hou, The influence of curing methods on the strength of MSWI bottom ash-based alkali-activated mortars: the role of leaching of OH– and free alkali, Constr. Build. Mater. 186 (2018) 978–985, https://doi.org/ 10.1016/j.conbuildmat.2018.07.224.
- [13] X. Yao, T. Yang, Z.Z. Zhang, Y. Wang, X. Liu, W.D. Zhang, Z. Li, Y. Zhang, Y. Li, Y. Ren, K. Sun, X. Peng, S. Wang, L. Zeng, P. Ran, G. Ji, M.A. Longhi, E. D. Rodríguez, B. Walkley, Z.Z. Zhang, A.P. Kirchheim, S.P. Kang, S.J. Kwon, X. Xue, Y.L. Liu, J.G. Dai, C.S. Poon, W.D. Zhang, P. Zhang, Z.Z. Zhang, J.L. Provis, X. Ma, A. Reid, H. Wang, J.L. Provis, A. Reid, X. Yao, T. Yang, Z.Z. Zhang, J.L. Provis, A. Reid, H. Wang, R.R. Lloyd, J.L. Provis, J.S.J. Van Deventer, Compressive strength development and shrinkage of alkali-activated fly ash–slag blends associated with efflorescence, Mater. Struct. 49 (2016) 165–177, https://doi.org/10.1016/j.cemconcomp.2018.06.010.
- [14] H. El-Hassan, E. Shehab, A. Al-Sallamin, Influence of different curing regimes on the performance and microstructure of alkali-activated slag concrete, J. Mater. Civ. Eng. 30 (2018) 4018230, https://doi.org/10.1061/(ASCE)MT.1943-5533 0002436
- [15] C. Liu, Y. Zhang, M. Liang, Z. Li, G. Ye, Underwater carbonation of alkali-activated slag pastes, Constr. Build. Mater. 445 (2024) 137967, https://doi.org/10.1016/j. conbuildmat.2024.137967.
- [16] M.H. Hubler, J.J. Thomas, H.M. Jennings, Influence of nucleation seeding on the hydration kinetics and compressive strength of alkali activated slag paste, Cem. Concr. Res. 41 (2011) 842–846, https://doi.org/10.1016/j. cemconres.2011.04.002.
- [17] H. Maghsoodloorad, A. Allahverdi, Efflorescence formation and control in alkaliactivated phosphorus slag cement, Int. J. Civ. Eng. 14 (2016) 425–438, https://doi. org/10.1007/s40999-016-0027-0.
- [18] C.L. Hwang, D.H. Vo, V.A. Tran, M.D. Yehualaw, Effect of high MgO content on the performance of alkali-activated fine slag under water and air curing conditions, Constr. Build. Mater. 186 (2018) 503–513, https://doi.org/10.1016/j. conbuildmat.2018.07.129.
- [19] C.H.W.Z.L.H.S.G.Y. Liu, Effect of Curing Condition on Mechanical Properties and Durability of Alkali-activated Slag Mortar, (2020) 1934472.
- [20] B.S.I. NEN-EN, 196-1. Methods of Testing Cement—Part 1: Determination of Strength, BSI London, UK. (2016).
- [21] W. Gardner, Note on the dynamics of capillary flow, Phys. Rev. 18 (1921) 206–209, https://doi.org/10.1103/PhysRev.18.206.
- [22] K.K. Aligizaki, Pore Structure of Cement-based Materials: Testing, Interpretation and Requirements, CRC Press, 2005.
- [23] R. Chaube, T. Kishi, K. Maekawa, Modelling of Concrete Performance: Hydration, Microstructure and Mass Transport, CRC Press, 1999.
- [24] J. Zhou, Performance of Engineered Cementitious Composites for Concrete
- [25] Y. Ma, J. Hu, G. Ye, The pore structure and permeability of alkali activated fly ash, Fuel 104 (2013) 771–780, https://doi.org/10.1016/j.fuel.2012.05.034.
- [26] B. Zheng, T. Li, H. Qi, L. Gao, X. Liu, L. Yuan, 3D meso-scale simulation of chloride ion transportation in cracked concrete considering aggregate morphology, Constr.

- Build. Mater. 326 (2022) 126632, https://doi.org/10.1016/j.conbuildmat.2022.126632.
- [27] Y. Li, X. Chen, L. Jin, R. Zhang, Experimental and numerical study on chloride transmission in cracked concrete, Constr. Build. Mater. 127 (2016) 425–435, https://doi.org/10.1016/j.conbuildmat.2016.10.044.
- [28] M. Belhocine, Y. Bouafia, M.S. Kachi, K. Benyahi, Assessment of non-linear behavior and ductility of reinforced concrete structures, World J. Eng. 20 (2023) 522–543, https://doi.org/10.1108/WJE-03-2021-0181.
- [29] B. Hillemeier, H.K. Hilsdorf, Fracture mechanics studies on concrete compounds, Cem. Concr. Res. 7 (1977) 523–535, https://doi.org/10.1016/0008-8846(77) 90114-4.
- [30] Z.P. Bažant, Concrete fracture models: testing and practice, Eng. Fract. Mech. 69 (2001) 165–205, https://doi.org/10.1016/S0013-7944(01)00084-4.
- [31] M.R. Pandimani, Y. Ponnada, Geddada, A comprehensive nonlinear finite element modelling and parametric analysis of reinforced concrete beams, World J. Eng. 20 (2023) 150–177, https://doi.org/10.1108/WJE-04-2021-0212.
- [32] Z. Li, T. Lu, X. Liang, H. Dong, G. Ye, Mechanisms of autogenous shrinkage of alkali-activated slag and fly ash pastes, Cem. Concr. Res. 135 (2020) 106107, https://doi.org/10.1016/j.cemconres.2020.106107.
- [34] W. Chen, B. Li, J. Wang, N. Thom, Effects of alkali dosage and silicate modulus on autogenous shrinkage of alkali-activated slag cement paste, Cem. Concr. Res. 141 (2021), https://doi.org/10.1016/j.cemconres.2020.106322.
- [35] D. Coefficient, Simple model for alkali leaching from geopolymers: effects of raw materials and acetic acid concentration on apparent, Materials 14 (6) (2021) 1425.
- [36] S.-D. Wang, K.L. Scrivener, Hydration products of alkali activated slag cement, Cem. Concr. Res. 25 (1995) 561–571, https://doi.org/10.1016/0008-8846(95) 00045-E.
- [37] M. Ben Haha, B. Lothenbach, G. Le Saout, F. Winnefeld, Influence of slag chemistry on the hydration of alkali-activated blast-furnace slag - part I: effect of MgO, Cem. Concr. Res. 41 (2011) 955–963, https://doi.org/10.1016/j. cemconres.2011.05.002.
- [38] Y. Zhang, S. Zhang, C. Liu, O. Çopuroğlu, Characterizing two types of zonation within slag rims of aged alkali-activated slag pastes through SEM and TEM, Cem. Concr. Res. 176 (2024) 107409, https://doi.org/10.1016/j. cemconres.2023.107409.
- [39] Z. Jia, C. Chen, H. Zhou, Y. Zhang, The characteristics and formation mechanism of the dark rim in alkali-activated slag, Cem. Concr. Compos. 112 (2020) 103682, https://doi.org/10.1016/j.cemconcomp.2020.103682.
- [40] I.G. Richardson, G.W. Groves, Microstructure and microanalysis of hardened cement pastes involving ground granulated blast-furnace slag, J. Mater. Sci. 27 (1992) 6204–6212, https://doi.org/10.1007/BF01133772.
- [41] I. Garcia-Lodeiro, A. Palomo, A. Fernández-Jiménez, D.E. MacPhee, Compatibility studies between N-A-S-H and C-A-S-H gels. Study in the ternary diagram Na2O-CaO-Al2O3-SiO 2-H2O, Cem. Concr. Res. 41 (2011) 923–931, https://doi.org/ 10.1016/j.cemconres.2011.05.006.
- [42] J. Li, W. Zhang, P.J.M. Monteiro, Structure and intrinsic mechanical properties of nanocrystalline calcium silicate hydrate, ACS Sustain. Chem. Eng. 8 (2020) 12453–12461, https://doi.org/10.1021/acssuschemeng.0c03230.
- [43] C. Liu, Z. Li, S. Nie, S. Skibsted, G. Ye, Structural evolution of calcium sodium aluminosilicate hydrate (C-(N-)A-S-H) gels induced by water exposure: the impact of Na leaching, Cem. Concr. Res. 178 (2024), https://doi.org/10.1016/j. cemconres.2024.107432.
- [44] C. Liu, Z. Li, G. Ye, Mechanisms of efflorescence of alkali-activated slag, Cem. Concr. Compos. 155 (2025) 105811, https://doi.org/10.1016/j. cemconcomp.2024.105811.
- [45] Y. Wang, Y. Cao, Z. Zhang, J. Huang, P. Zhang, Y. Ma, H. Wang, Study of acidic degradation of alkali-activated materials using synthetic C-(N)-A-S-H and N-A-S-H gels, Compos. Part B Eng. 230 (2021) 109510, https://doi.org/10.1016/j. compositesb.2021.109510.
- [46] F. Spectroscopy, Structure of calcium silicate hydrate (C-S-H): near-, mid-, and far-infrared, Spectroscopy 48 (1999) 742–748.
- [47] A.J. Katz, A.H. Thompson, Quantitative prediction of permeability in porous rock, Phys. Rev. B 34 (1986) 8179.
- [48] T.C. Powers, L.E. Copeland, H.M. Mann, Capillary Continuity or Discontinuity in Cement Pastes, 1959.
- [49] L. Cui, J.H. Cahyadi, Permeability and pore structure of OPC paste, Cem. Concr. Res. 31 (2001) 277–282, https://doi.org/10.1016/S0008-8846(00)00474-9.
- [50] J.M. Whitney, M. Knight, The relationship between tensile strength and flexure strength in fiber-reinforced composites: flexure-and tensile-coupon data on unidirectional graphite-epoxy composites are compared to a weibull twoparameter statistical-strength model, Exp. Mech. 20 (1980) 211–216.
- [51] M.R. Wisnom, The relationship between tensile and flexural strength of unidirectional composites, J. Compos. Mater. 26 (1992) 1173–1180.
- [52] C. Liu, W. Haoming, L. Zhenming, S. Hu, Y. Guang, Effect of curing condition on mechanical properties and durability of alkali-activated slag mortar, Constr. Build. Mater. 439 (2024) 137376, https://doi.org/10.1016/j.conbuildmat.2024.137376.
- [53] C. Liu, Y. Tao, S. Nie, Y. Chen, Z. Li, C.S. Poon, G. Ye, Dissolution of cations in C-(N, K-)A-S-H gels at the nanoscale, Compos. Part B Eng. ISSN: 1359-8368 297 (2025) 112337, https://doi.org/10.1016/j.compositesb.2025.112337.